ISTITUTO NAZIONALE DI RICERCA METROLOGICA
Repository Istituzionale

Magnetic Nanoparticle Imaging: Insight on the Effects of Magnetic Interactions and Hysteresis of Tracers

(Article begins on next page)

26 November 2024

Magnetic Nanoparticle Imaging: Insight on the Effects of Magnetic Interactions and Hysteresis of Tracers

Gabriele Barrera,* Paolo Allia, and Paola Tiberto

Advanced materials metrology and life sciences, INRiM, Torino, Italy

E-mail: g.barrera@inrim.it

Abstract

The dynamic properties of magnetite nanoparticles are investigated by rate equations with the aim of clarifying the factors affecting their performance as tracers in magnetic particle imaging (MPI). It is shown that size-dependent effects such as magnetic hysteresis and dipole-dipole interaction may have a great impact on the behaviour of MPI tracers. Usually, magnetic imaging exploits higher-order harmonics of the magnetization waveform without considering either intra-particle hysteresis or inter-particle interactions. These assumptions may result in an incorrect estimate (either by excess or by defect) of nanoparticle concentration, which is the ultimate aim of MPI. The mismatch between real and estimated values is apparent for concentrations typical of some therapeutic applications of magnetic nanoparticles, or reached by effect of particle accumulation in organs owing to slow clearance processes. We show that this difficulty can be removed measuring not only the magnitude of the third harmonic of the signal but also the phase shift with respect to the driving field. The proposed technique of signal adjustment makes use of the settings of present-day MPI operating devices. The validity of the adjustment procedure is checked by a proof of concept using non-uniform nanoparticle concentrations.

Introduction

Magnetic Particle Imaging (MPI) has emerged as a novel tomographic technique[1–4] with widespread prospective applications in bio-medicine[5–8] both as a standalone method of diagnostic imaging[9–13] and as an auxiliary diagnostic tool associated to specific therapies of precision medicine.[14–17]

MPI is based upon the detection and analysis of the voltage induced by magnetic tracers at the nanoscale (usually based on iron oxide nanoparticles as already approved by the US Food and Drug Administration (FDA) for human use[18]) under the combined action of a high-frequency sinusoidal magnetic field $H(t)$ and of a non-uniform magnetic field characterized by a high gradient (called bias field).[3,10,19,20] The technique has the double advantage of not requiring the use of ionizing radiation and of penetrating tissues deeply inside a living body[6,21] (such a property being shared with the related technique of Magnetic Particle Spectroscopy[22,23]). MPI takes further advantage from the present-day knowledge on diffusion, steering, positioning and clearance of magnetic nanoparticles inoculated in a living body.[24–26]

Accurate localization of nanoparticles within a target tissue is mandatory in the therapeutic practice,[24,27,28] and can be properly achieved by means of MPI. In fact, when the bias-field gradient is sufficiently large only the tracers placed where the bias field is zero have their magnetic state dynamically modified by the driving field $H(t)$ and generate the MPI signal; in actual devices the active region can be either a very small area (a point) or an entire narrow strip (a line) which are called field-free point/line (FFP/FFL), respectively.[2,3] Nanotracers placed out of the active region can be assumed to be magnetically saturated by the bias field, which is no longer vanishingly small there, and therefore remain magnetically inert under the action of the driving field $H(t)$.

A parameter of primary importance in biomedicine is the local concentration of magnetic nanoparticles,[29] which should be very precisely estimated in all applications where the therapeutic efficiency is intrinsically related to a cumulative effect of nanoparticles. For

instance, in both magnetic hyperthermia and particle-assisted drug release a local concentration threshold can usually be defined, under which the healing effect is lost.[24,30–32] MPI is a powerful method for determining the local concentration of magnetic tracers in a living tissue.[3,5,9,11,28,33–35]

In all imaging techniques based upon detection of specific nanotracers by effect of the physical effects which take place in the nanotracers themselves, an in-depth knowledge of the underlying physics is needed.[28,36] In the case of MPI, the magnetic properties of tracers at the operation frequency should be known in great detail. However, the signal picked up by a MPI device is often interpreted on the basis of a very simplified description of the physical principles which take place in magnetic nanoparticles and govern their behaviour under the driving field.[2,3,19,37]

Usually, magnetic tracers eligible for MPI are described as being in the ideal superparamagnetic state at room temperature, which means that the magnetic response to the driving field is fully reversible, albeit definitely nonlinear.[2,3,19,37] The intrinsic nonlinearity of the magnetic response is the key factor to build a MPI map of the scanned tissue. Usually, a MPI device works by detecting higher-order harmonics of the induced signal, which is in turn proportional to the magnetization $M(t)$ of particles driven by a sinusoidal field $H(t)$ of frequency f. The $M(t)$ waveform is non-sinusoidal because of the nonlinearity existing between M and H, and contains higher-order odd harmonics of frequencies equal to $3f$, $5f$,.., the third harmonic being obviously the largest and the one usually exploited in actual devices.[2,3,34]

However, the current description of the magnetic tracers as ideally superparamagnetic particles loses a great deal of meaning at high frequencies such as the ones typically used in MPI (10-100 kHz), a circumstance often not duly taken into account.[9,38,39] A more insightful description of the magnetic response of tracers at high frequency is needed, although this may be a challenging task owing to the existence of magnetic hysteresis effects which can make the magnetic response of an assembly of nanoparticles more complex.[40,41] Magnetic

hysteresis in nanoparticles is influenced by various factors including size, morphology,[42] surface functionalization[43] and affects the efficiency of the MPI response of actual nanoparticle dispersions.

Another type of difficulties arises from neglecting the magnetic interactions among particles, which again emerge by effect of particle size, morphology, surface functionalization and nanoparticle concentration[31,42,43]. Often magnetic nanoparticles used as tracers for MPI are considered as virtually noninteracting. Although this is a good approximation for small nanoparticles and very low tracer concentrations, as is indeed the case in specific applications of MPI,[9,11,14,34,44] this is not the general rule.[45,46] There are many practical cases where the nanoparticle concentration in a living tissue can become high enough that magnetic interactions can no longer be neglected. This applies, for instance, to MPI-guided magnetic hyperthermia, where nanoparticles have to accumulate in correspondence of the target tissue in order to produce the desired heating effect.[14,17,47] Even in applications where the concentration of nanoparticles capable of providing therapeutic effects is low on the average, locally high concentrations can be found in tissues and/or organs by effect of a slow process of nanoparticle clearance and excretion, possibly resulting in dangerous side effects.[48–50] It should be noted that dipole-dipole interaction among particles exists even when the particles are well separated from each other[51], as recently checked in a suspension of commercial iron-oxide nanoparticles.[52] Dipolar interaction can be simply modeled, and is shown to be proportional to particle concentration;[31,53,54] at high frequencies the interaction becomes non-negligible when the mean interparticle distance is lower than three to four times the nanoparticle diameter.[31,54]

This paper is aimed to closely inspect the factors affecting the magnetic response of realistic assemblies of magnetite nanotracers submitted to a sinusoidal driving field of magnitude and frequency appropriate to typical MPI operations.

Generally speaking, the magnetic behaviour of nanoparticles in living tissues is influenced by the specific environment where they are placed.[55,56] At the typical operating frequencies of

MPI, Brown's magnetic relaxation[57] can be safely taken as negligible with respect to Néel's magnetic relaxation,[57] at least when when the physical degrees of freedom of NPs in space are almost suppressed as often observed in living tissues.[55,58] This is precisely the scenario addressed to in the present paper.

The model makes use of a consolidated technique based on magnetic rate equations.[31,41,59–62] It is shown that the complex magnetic effects arising in an assembly of magnetite nanoparticles (including magnetic hysteresis and interactions) pose a real challenge to the conventional use of the third harmonic as a reliable tool to measure the real concentration of tracers at the FFP. In particular, we find that in interacting systems the estimate of tracer concentration which results from the standard procedure can be significantly different (either by excess or by defect) from the real value. Such a mismatch can result in a therapeutic action potentially ineffective or even harmful to a patient.

However, it is also shown that making a full use of the information contained in the third harmonic of the signal (basically, measuring not only its magnitude but also the phase shift with respect to the driving field) it is possible to give a satisfactory solution to this problem by means of a technique of signal adjustment which makes use of the same type of settings currently used by present-day MPI operating devices, as summarized by Scheme 1. Using the phase shift between magnetization and driving field as an alternative parameter to get independent information from MPI tracers is still a rather uncommon practice, although this quantity has been exploited in some systems where Brown's relaxation is predominant.[63,64]

Model: magnetic hysteresis of interacting nanoparticles

The model of nanoparticle magnetization is based upon a system of rate equations whose solution gives the time-resolved occupancy numbers of potential-energy wells corresponding to the two minima of the effective magnetic anisotropy energy of a single nanoparticle, assumed to be a double level system (DWS).[41,65] Generally speaking, at any finite temperature the oc-
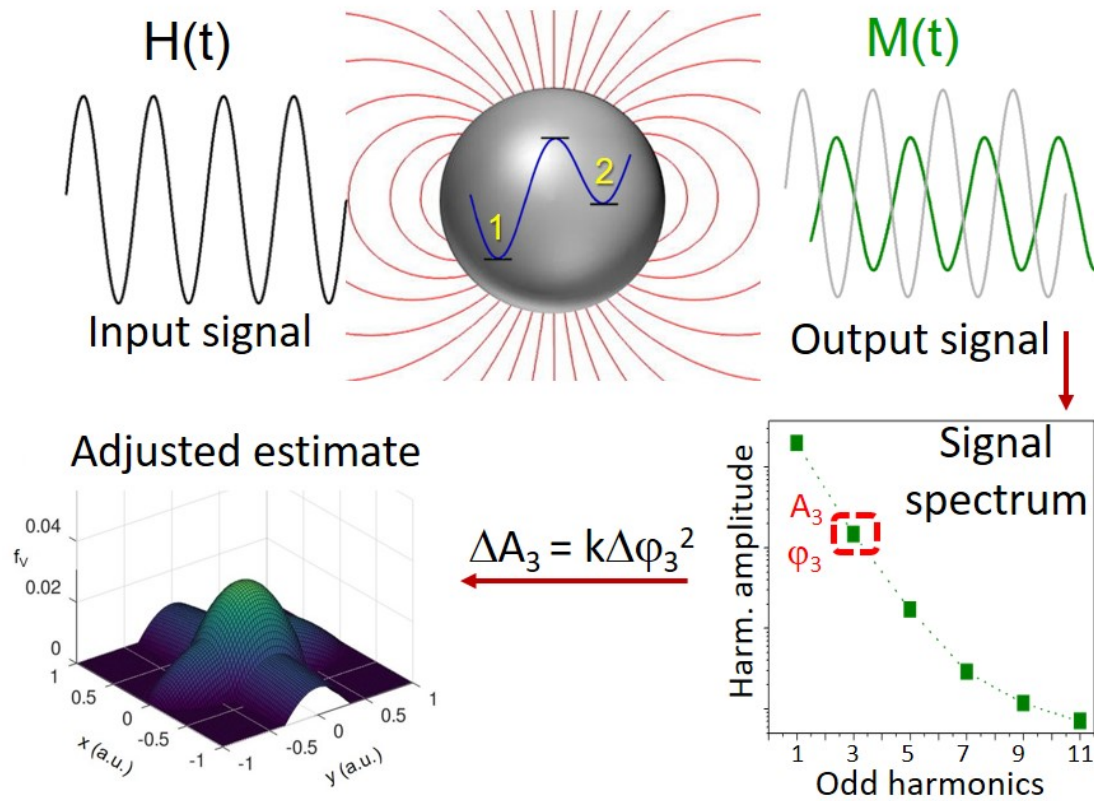
Scheme 1: Interacting magnetite nanoparticles described as two-level systems and submitted to a high-frequency driving field generate a non-harmonic magnetic response which is analysed in frequency; a relation between amplitude and phase of the third harmonic is exploited to get the correct estimate of the local concentration of nanotracers.

cupancy numbers of the two wells can change by effect of thermally activated jumps over the barrier between wells and are triggered by the applied magnetic field also.[41] The calculations are done for all angles ϕ between the nanoparticle's easy axis and the instantaneous magnetic field direction. The overall magnetization of an assembly of nanoparticles with random easy axes is obtained by summing up the output of the rate equations for each ϕ and can be plotted as a function of either time or magnetic field. Properties, advantages and application limits of the rate-equation method applied to the dynamics of nanoparticle magnetization in the intermediate frequency range (below about 500 kHz) have been extensively discussed in a number of papers[31,41,61,62,66] and are reported in brief as Supporting Information. In the present rate-equation approach, it is pure Néel relaxation that determines the evolution of particle magnetization, Brown's mechanism not being considered by definition. In these conditions, the amplitude of the magnetic response of a set of nanoparticles is expected to drop to zero above a critical particle size whose value critically depends on frequency, temperature, magnetic anisotropy.[62,67] Such a scenario happens when MPI tracers inside the target tissue are physically immobilized.[55,58] For typical magnetite nanoparticles the upper limit of the size interval where Néel relaxation mechanism acts is around 15-16 nm at 25 kHz and at room temperature. Of course, an efficient response of MPI tracers can be observed even above that size limit when the particles are placed in an acqueous medium, provided that the values of the viscosity and the particle's hydrodynamic radius allow for substantial Brown's relaxation to occur.[67] For instance, the optimal performance at 25 kHz observed in 20-nm iron oxide particles with a hydrodynamic radius of 30 nm[68] can be ascribed to pure Brown's relaxation, so that the same particles, when immobilized, would give no detectable MPI signal.[69] Similar considerations also apply to particle aggregates or multi-core beads, which usually can be pictured as large magnetic units composed of individual particles of smaller size.[67,70]

In the rate-equation framework, a central role is played by the effective energy barrier

7

between the two potential-energy wells, E_B, which is determined not only by the particle's magnetic anisotropy but also by a term taking into account the dipolar interaction among nanoparticles.[31] For monodisperse nanoparticles of size D and volume $V = (\pi/6)D^3$ characterized by uniaxial magnetic anisotropy of magnitude K_u whose easy axis makes an angle ϕ with the magnetic field, the following expression has been proposed for the energy barrier seen by well i (i=1,2) of the double-well system:

$$E_{B\,i}(H.\phi) = E_{B\,i}^0(H, \phi) + \alpha M_s^2 V \left(1 - \frac{|m_0|}{2}\right) f_V. \tag{1}$$

where M_s is the particle's saturation magnetization, $f_V = 1/d^3$ is the concentration of particles placed in a definite region of the host medium (either biological or not), d is the mean interparticle distance, $E_{B\,i}^0(H, \phi)$ is the barrier's height for the non-interacting system, $|m_0|$ is the absolute value of the reduced magnetization, α is a dimensionless constant of the order of magnitude of 10. The magnitude of $E_{B\,i}^0(H = 0, \phi)$ is primarily determined by the product $K_u V$; the usual Zeeman-energy term adds to $K_u V$ when the magnetic field is switched on. In this model, dipolar interaction modifies the energy barrier of each DWS, making it possible to reduce a many-body problem to a mean-field theory.[31] The model is based on a statistical description of the dipolar energy in an ensemble of magnetic nanoparticles[71] and bears close similarities with other approaches[57,72] based on a different expression of the same energy, basically equivalent at fixed temperature to the one used here[72]. The energy barrier determines the values of the time constants appearing in the rate equations, τ_i:

$$\tau_i = \tau_0 \, exp \left[\frac{E_{B\,i}}{k_B T}\right] \tag{2}$$

where $\tau_0^{-1} \simeq 10^{-9}$ s^{-1} is the attempt frequency, k_B is the Boltzmann constant and T the temperature. The reciprocal of each time constant τ_i (i =1,2) is the escape frequency out of well i. In this paper the following values of the magnetic parameters, appropriate to magnetite nanoparticles at room temperature, are used: M_s = 350 emu/cm^3; K_u = 3×10^5

erg/cm^3. The particle diameters are in the 11 - 16 nm range; this choice ensures that the rate equations can be safely applied at room temperature and at the working frequency of 25 kHz.[61,73]

The overall energy barrier for interacting particles is linearly dependent on f_V, implying that the kinetics of redistribution of nanoparticles in the potential wells and the magnetic response of the system are critically affected by the fraction of particles present in the unit volume of the host medium. It should be noted that in this model noninteracting nanoparticles are described in the limit $f_V \to 0$ $(d \to \infty)$.

Depending on various factors (nanoparticle size, temperature, driving field frequency, nanoparticle concentration) the system's magnetization M plotted as a function of the magnetic field H can either display a hysteresis loop or be anhysteretic, basically reducing to a Langevin curve. When all the other parameters are kept constant, a central role is played by the driving field frequency, which is usually in the 10 - 500 kHz range in biomedicine applications.[29,74] In particular, MPI makes use of a frequency of the order of 20-30 kHz.[3,19] Often, such terms as "superparamagnetic state" (no magnetic hysteresis) or "blocked state" (presence of hysteresis) are associated to the magnetic behaviour of a nanoparticle in dc measurements, i.e., at almost zero frequency. However, particular attention should be payed when operating at higher driving-field frequencies.

A typical example of the changes introduced by a high magnetizing frequency is shown in panels a), b) of Figure 1, where the room-temperature magnetization of two nanoparticle assemblies with random easy axes is reported as a function of H. For the sake of simplicity, the nanoparticles are assumed to be noninteracting and monodisperse. The time dependence of the driving field is $H(t) = H_V cos(\omega t)$ with $\omega = 2\pi f$. The maximum amplitude of the harmonic field (H_V) is called "vertex field".

In panel a) the frequency is vanishingly small, and the resulting $M(H)$ curves for both particle sizes turn out to be nonhysteretic in the region $|H| \leq H_V$ (full lines; the dashed
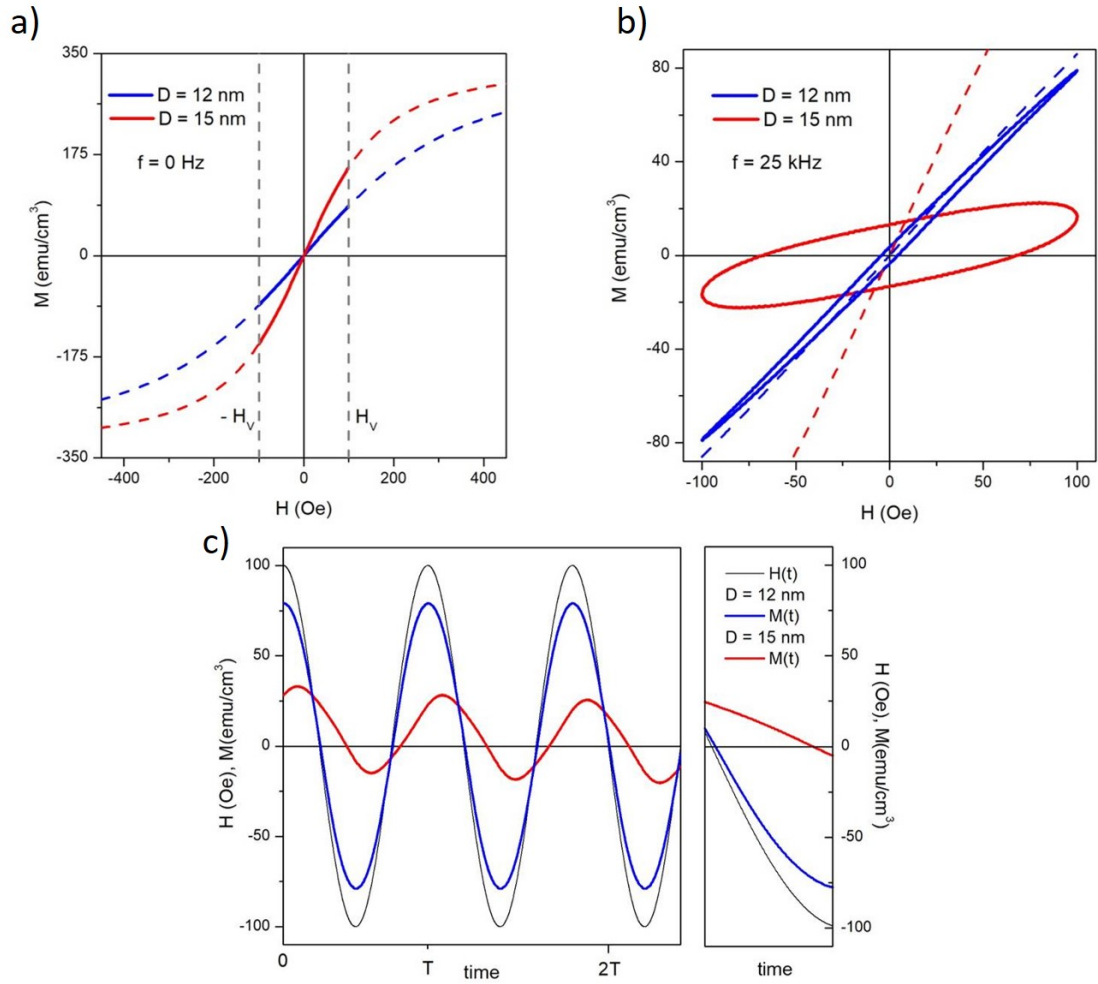
Figure 1: (a): Full lines: anhysteretic magnetization of two monodisperse nanoparticle assemblies in quasi-static conditions for $H \leq H_V = 100$ Oe; dashed lines: Langevin curves; (b): magnetic hysteresis in the same systems under a high-frequency driving field of vertex H_V; dashed lines: Langevin curves; (c): $H(t)$ (thin black line) and $M(t)$ waveforms (thick lines in colour) at 25 kOe. The phase shifts of $M(t)$ are shown in the rightmost bottom panel.

lines show the Langevin curves over an extended field interval). In this case the rate equations predict complete reversibility of the magnetic response independently of particle size. According to the standard practice, both types of nanoparticles can be termed as "superparamagnetic". However, when a higher frequency of $H(t)$ is used (25 kHz, as in panel b)), hysteresis loops appear. In the case of particles with $D = 12$ nm a slender, narrow loop is observed and the cyclic magnetization never takes values much different from the ones predicted by the corresponding Langevin curve (dashed blue line); in the case of 15-nm particles, however, a much wider loop appears and the cyclic magnetization is now very different from the Langevin curve (red dashed curve),

The hysteretic magnetization which emerges when operating at high frequencies is naturally related to the rapidity of the change of H with time, which can be followed with smaller or larger delay by the nanoparticles. In fact, the response of a particle is determined by the time constants τ_i of the rate equations (typically larger in larger nanoparticles because of the higher energy barrier involved).[41,65] The delay between $H(t)$ and $M(t)$ is responsible for the hysteresis loop observed when M is plotted as a function of H. The time-resolved solutions of the rate equations at $f = 25$ kHz are shown in panel c) of Figure 1 for the two nanoparticle sizes, along with the driving field waveform (black line). The larger delay of the cyclic magnetization of 15-nm nanoparticles with respect to $H(t)$ (clearly evidenced by the rightmost panel) is associated with the wider hysteresis loop observed in panel b).

When magnetic hysteresis is present, the signal $M(t)$ - or alternatively the induced voltage $V \propto -dM/dt$ - is characterized not only by a deformed waveform but also by a phase shift with respect to the driving field. Indeed, such a phase shift is the real hallmark of the presence of magnetic hysteresis. On the contrary, no phase shift is observed in the signal produced by ideal superparamagnetic particles whose magnetization is given by the Langevin function, which is a fully reversible function of H.

On the other hand, properly tuning the strength of the dipolar interaction among nanoparticles can affect the shape of the hysteresis loops as well. In our model, both the strength

of dipolar interaction and the barrier height linearly increase with increasing the volume concentration of nanoparticles. The effect is shown in Figure 2a, where three loops, corresponding to increasing vales of f_V, are shown for monodisperse nanoparticles with $D = 12$ and 15 nm.

The vertex field is again $H_V = 100$ Oe and the operating frequency $f = 25$ kHz. The upper limit of the particle concentration range is taken at $f_V = 0.03$ ($\equiv 3\%$ vol), in line with the practical applications *in-vivo*[75] and in preclinical MPI experiments.[76] For the larger particle size the effect of switching the interaction on is stronger. Even more important, the hysteresis loop can become either wider or narrower than in the noninteracting case, depending on nanoparticle size. This interesting effect, which has dramatic consequences on the heating ability of magnetic nanoparticles, has been explained in detail elsewhere[31] and is basically related to the fact that for a given particle size there is one and only one value of the energy barrier E_B (and hence of f_V) corresponding to the maximum width of the hysteresis loop. In particular, the loop area takes the maximum value when E_B is such that

$$\tau \equiv \tau_0 \, \exp\left[\frac{E_B}{k_B T}\right] \simeq \frac{1}{2f} \tag{3}$$

E_B being the average of the barriers for the two wells, $E_{B,1}$ and $E_{B,2}$.

Magnetic hysteresis in the MPI operating practice

High-frequency response of magnetic nanoparticles

MPI is typically based upon the detection of the third harmonic of the induced voltage produced in a small region of living tissue containing magnetic nanoparticles. The third harmonic of the signal is the fingerprint of the presence of nanoparticles. The simplest way to prove this is to assume a superparamagnetic behaviour: the nonlinearity of the Langevin function with the field naturally results in a magnetic response where all odd higher-order
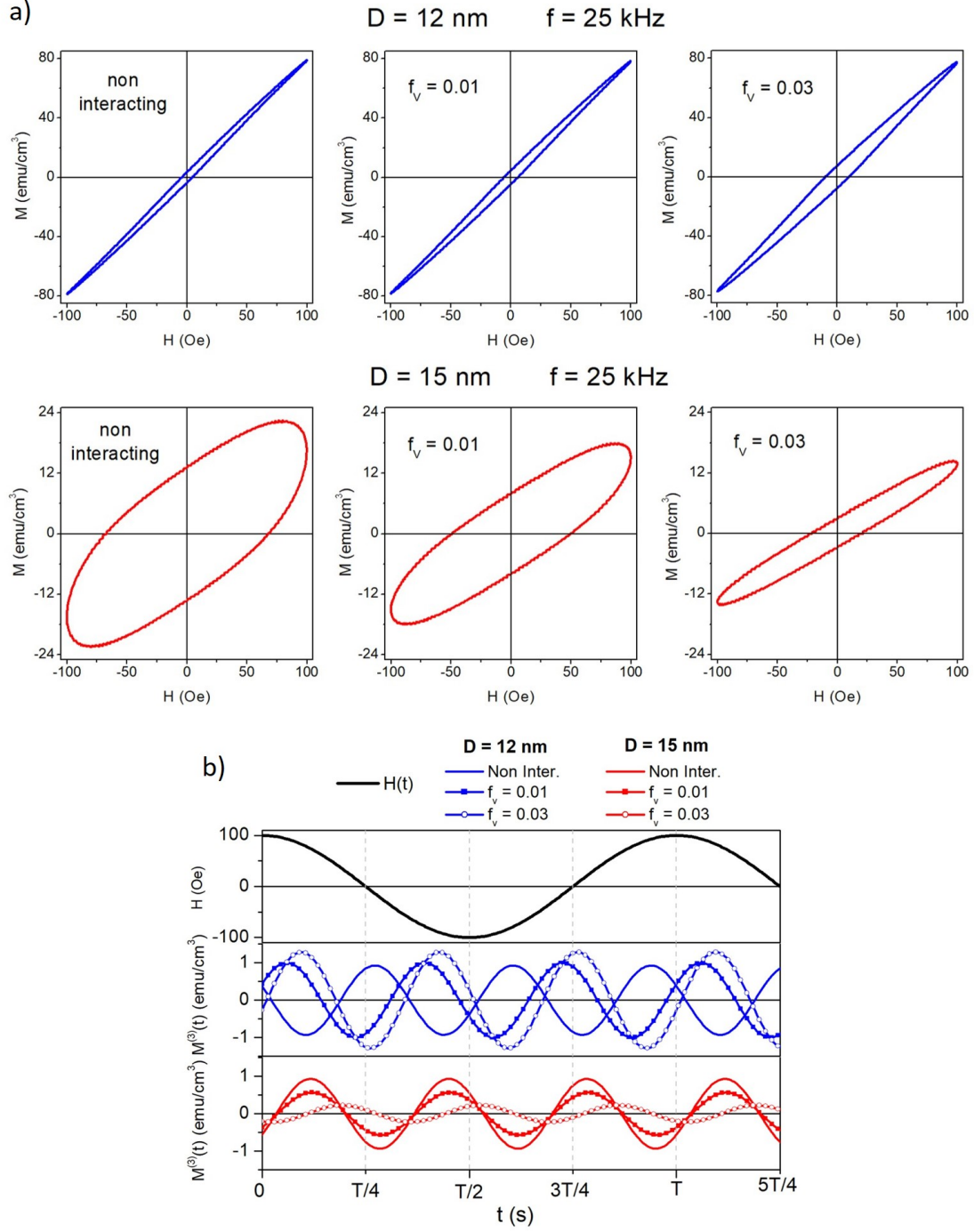
Figure 2: a) Effect of dipolar interaction (measured by particle concentration f_V) on the shape of magnetic hysteresis loops at 25 kOe. Upper row: 12-nm particles; lower row: 15-nm particles; b) from top to bottom: harmonic $H(t)$ waveform; third harmonic of $M(t)$ for $D = 12$ nm particles with three different degrees of interaction; the same for $D = 15$ nm particles.

harmonics are present.

The MPI signal comes from the active region where the bias field is close to zero; the steeper the gradient of the bias field, the more accurate is the measurement. For this reason, in this paper the magnetic response is always investigated at the FFP of an ideal MPI setup.

Usually, magnetic nanoparticles are traced using the magnitude of the third harmonic of the signal, whilst the phase shift with respect to the driving field is neglected. This would be entirely correct if the particles were superparamagnetic: a fully reversible $M(H)$ curve corresponds to a $M(t)$ waveform exactly in phase with the driving field. However, as we have shown, a hysteresis loop is observed in high-frequency measurements even in nanoparticles which are superparamagnetic in dc measurements. When the loop opens, a phase shift of all odd harmonics of the picked-up signal is observed.

An example is given in Figure 2b: the upper row shows the driving field ($H_V = 100$ Oe), whilst the two lower rows show $M^{(3)}(t)$, the third harmonic of $M(t)$, for two monodisperse nanoparticle systems ($D = 12$ and 15 nm) treated as either noninteracting or interacting (using two different values of f_V). All parameter values in Figure 2b are the same as the ones used in Figure 2a in order to ease the comparison between the evolution of the third harmonic and the loop shape. Figure 2b shows how magnetic hysteresis affects both magnitude (M_3) and phase shift (ϕ_3) of the third harmonic: a) magnetic interactions, leading either to an increase of a decrease of the loop area (Figure 2a), act to either enhance ($D = 12$ nm) or reduce ($D = 15$ nm) the magnitude M_3 with respect to the noninteracting case; b) the third harmonic of $M(t)$ always displays a phase shift with respect to $H(t)$, clearly indicating that the $M(H)$ curve is not reversible; the phase shift is further modified by dipolar interaction.[4]

The rate-equation model explains why the efficiency of magnetic nanoparticles as MPI tracers is limited to a narrow range of sizes (typically between 10-11 nm and 16-17 nm for

---

[4]In this paper, the focus is on $M^{(3)}(t)$, the third harmonic of $M(t)$, rather than on the third harmonic of the induced voltage $V(t) \propto -dM/dT$, which is the actual output of a typical MPI measuring device. In fact, the magnitudes of the two quantities are directly proportional to each other, and their phase shifts merely differ by a $\pi/2$ term.

magnetite particles using the present parameter values). In fact, the magnetization vs. field curve of small particles at 25 kHz is basically given by the Langevin function; as a consequence, it is in phase with the driving field and the magnitude of its third harmonic becomes negligible for this vertex field;[3] on the contrary, the magnetic response of large particles submitted to pure Néel relaxation is basically linear with $H(t)$, so that the third harmonic and the associated phase shift are both vanishingly small.

MPI signal from a living tissue

In MPI, the magnitude of the third harmonic is typically used to measure the concentration of nanoparticles in a living tissue or organ. It should be noted that if M_3 is the magnitude of the third harmonic generated by magnetic nanoparticles, the quantity actually measured by a MPI device on a system of nanoparticles of concentration f_V dispersed in a non-magnetic host is $A_3 = M_3 f_V$.

The MPI measuring setup needs to be suitably calibrated; calibration is usually done by measuring the third harmonic of the signal $A_3^{(c)} = M_3 f_V^{(c)}$ from a sample containing a known concentration $f_V^{(c)}$ (usually very small) of magnetic nanoparticles. In this way, the angular coefficient $h = A_3^{(c)}/f_V^{(c)}$ of a straight line (calibration line) is obtained, allowing one to associate the A_3 value measured on a real target to a specific f_V^* value through the linear relation $A_3 = hf_V$ (green line in Figure 3).

However, such a procedure is inherently based upon the assumption of ideally noninteracting particles. In all cases where a local accumulation (either intentional or unintentional) of nanoparticles exists, interaction effects can play an important role and cannot be neglected.

Although increasing f_V modifies the energy barrier E_{Bi} in a linear way (Eq. 1), the barrier goes to the exponent of the time constants τ_i (Eq. 2). The presence of highly non-linear terms in the rate equations implies that the magnetization of an assembly of interacting nanoparticles cannot be described by simple analytic expressions (for the analytic treatment

of a special case, see the Appendix). The shape of the $M(H)$ curve for noninteracting particles - which at high frequencies is in general already hysteretic - is always modified by adding the dipolar interaction term, so that both magnitude and phase shift of the third harmonic of $M(t)$ change, as already observed in Figure 2b.
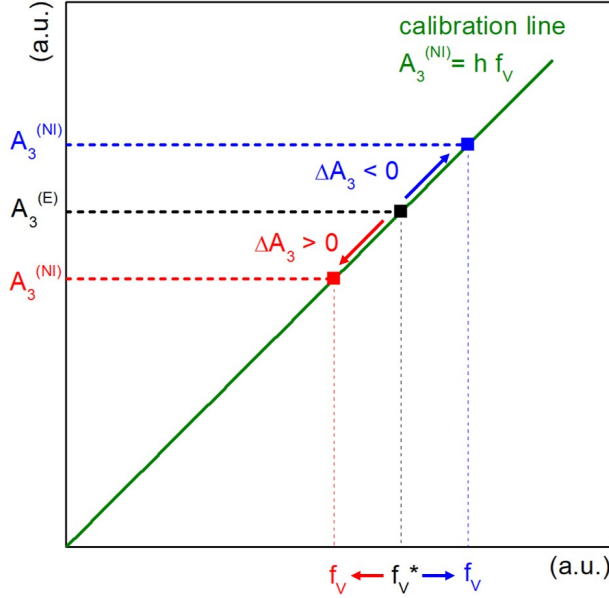

Figure 3: Connection between measured magnitude of the third harmonic $A_3^{(E)} = M_3 f_V$ and particle concentration at the target's FFP (f_V^*). Associating f_V^* to $A_3^{(E)}$ through the calibration line works only for noninteracting particles. When particles interact, the real concentration f_V can be either larger (blue symbols) or smaller (red symbols) than f_V^*. See text for details.

One important consequence of this change of hysteretic properties is that when nanoparticles are interacting the magnitude of the quantity $A_3 = M_3 f_V$ is no longer a linear function of f_V. The effect is apparent in the two upper panels of Figure 4.

There, the linear behaviour of A_3 with f_V predicted when the particles are ideally noninteracting (dashed lines) is compared with the actual behaviour of the same quantity obtained after solving the rate equations. Some different cases are studied in order to assess the effect of particle size on the correction. All curves initially follow a linear law, as expected when dipolar interaction is negligible; however, they soon depart from the straight line: for smaller D values (left upper panel) A_3 turns out to be higher than the one predicted by the linear
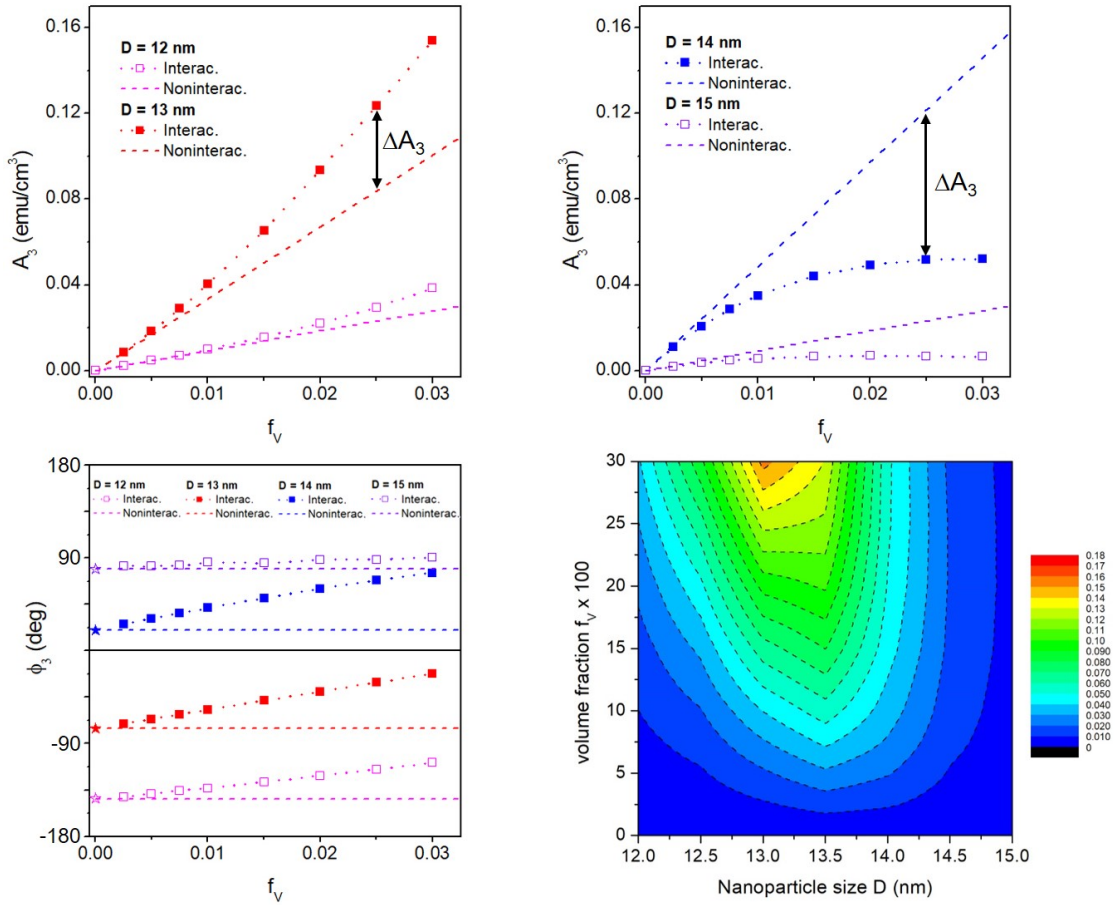
Figure 4: Upper panels: behaviour of the magnitude of the third harmonic of the signal $(A_3 = M_3 f_v)$ as a function of particle concentration f_V in monodisperse assemblies with different particle diameters. Lower right panel: behaviour with f_V of the phase shift ϕ_3. Lower right panel: contour map evidencing the combined effect of particle size and volume fraction on A_3.

law; for larger D values, the opposite behaviour is obtained. This means that the correction is critically dependent, in magnitude and sign, on particle size.

The behaviour of A_3 derives from the variation of M_3 with size D when magnetic hysteresis is present: a qualitative explanation of the opposite effects observed in smaller versus larger nanoparticles is based on the non-monotonic behaviour of $M_3(D)$ reported in Figure 5 for both noninteracting and interacting particles. The features of the $M_3(D)$ curve for noninteracting particles (black line in Figure 5) can be interpreted making reference to an analytical treatment for an assembly of particles whose easy axes are parallel to each other and to the applied field direction (collinear system). In this special case the rate equations can be analytically solved as shown in the Appendix, and an explicit expression for the diameter $D^{(max)}$ corresponding to the maximum of the $M_3(D)$ curve is obtained. For noninteracting collinear particles:

$$D_{NI}^{(max)} = \left[\frac{6 k_B T}{\pi K_u} ln \left(\frac{\sqrt{5}}{3\pi} \frac{1}{f\tau_0} \right) \right]^{1/3}. \tag{4}$$

This expression holds even in the general case of particles with random easy axes. In fact, Eq. 4 gives $D_{NI}^{(max)} = 13.4$ nm, a value very close to the exact numerical solution for particles with random easy axes, $D_{NI}^{(max)} = 13.7$ nm (see Figure 5).

Increasing f_V brings about an almost rigid displacement of the $M_3(D)$ curve towards left, as shown in Figure 5. This explains why M_3 either increases or decreases with increasing f_V, depending on the value of D and the distance from the peak position. The transition from one regime to the other one is basically marked by $D_{NI}^{(max)}$: when $D < D_{NI}^{(max)}$ M_3 increases with f_V, the opposite being true for $D > D_{NI}^{(max)}$. This prediction is in agreement with recent experimental results[46] indicating that for large nanoparticles increasing the dipolar interaction brings about a decrease in magnetic performance of tracers, measured here by the decrease in magnitude of M_3. The analytical treatment of the Appendix explains the displacement of the maximum with f_V in terms of a linear relation which retains validity even in the general case of random easy axes:

$$\frac{D^{(max)}(f_V)}{D_{NI}^{(max)}} = 1 - \frac{\alpha M_s^2}{3K_u} f_V. \tag{5}$$

Eq. 5 describes very well the displacement toward left of the maximum of the M_3 curve with f_V which results from numerically solving the rate equations, as shown by the vertical arrows in Figure 5.
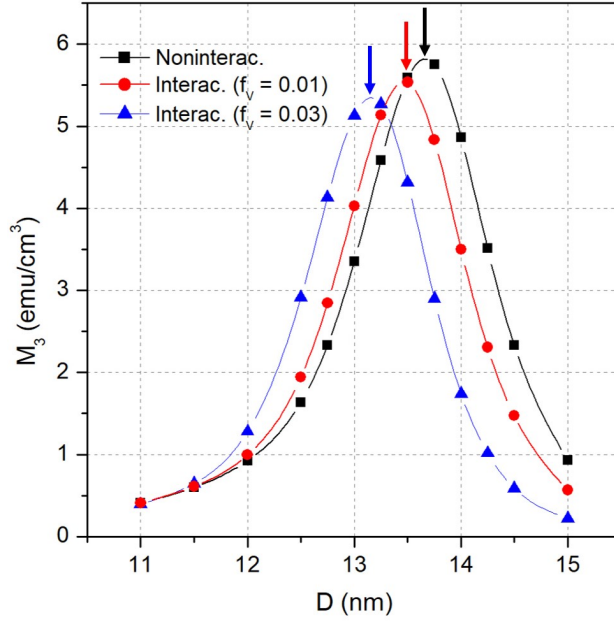

Figure 5: Magnitude of the third harmonic of the $M(t)$ signal as a function of particle diameter for different degrees of dipolar interaction. Arrows mark the position of the maximum as predicted by Eq. 5.

The difference observed for each f_V between the actual values of A_3 and the ones predicted by the linear theory is $\Delta A_3 \equiv \left[A_3 - A_3^{(NI)} \right]$, where $A_3^{(NI)}$ is the amplitude in the noninteracting case; two examples of this quantity are drawn in the two upper panels of Figure 4.

Increasing f_V also results in remarkable changes of the phase shift of the third harmonic ϕ_3, as shown in the lower left panel of Figure 4 for all investigated nanoparticle sizes. There, the horizontal dashed lines represent the behaviour in the absence of interactions (in which case, the phase shift is independent of f_V).

19

In all examined cases, a phase shift is already present for noninteracting particles, because they all display a hysteresis loop at 25 kHz. It should be remarked that the ϕ_3 values of noninteracting particles approach -180° with decreasing particle size, as indeed expected: when D is sufficiently small, magnetic hysteresis disappears even at these frequencies and the loop reduces to a reversible line. In this case the phase shift is predicted to be exactly -180° (see Supporting Information for a detailed explanation). In fact, the shift of ϕ_3 from -180° can be taken as a measure of how much does the actual $M(H)$ curve differ from the fully reversible Langevin function. This applies to the case of interacting particles too: the larger the particle size and/or the dipolar interaction, the larger is the distance of the loop's shape from the Langevin curve.

The effect of independently modifying D and f_V is shown in the lower right panel of Figure 4, where different colours in the contour map indicate different levels of A_3. For the explored ranges of particle sizes and concentrations (corresponding to the region of higher interest in applications), A_3 takes the maximum value when $D \simeq 13.5$ nm. The most notable feature of this contour map is that the maximum of the signal does not correspond to the maximum particle diameter in this size range, as predicted when the dependence of M on H is assumed to follow the anhysteretic Langevin law (in that case, the steeper the Langevin function, the higher is M_3; Figure 4 shows however that this is no longer true when the hysteretic properties of the $M(H)$ curve are properly taken into account).

The main consequence of the deviation of the $A_3(f_V)$ curve from the straight line is that the amplitude of the third harmonic is no longer a good measure of the real concentration of nanoparticles in the target tissue, as sketched in Figure 3. Only when the experimental magnitude $A_3^{(E)}$ is coincident with $A_3^{(NI)}$ the concentration obtained by using the calibration line (f_V^*) corresponds to the real concentration. In the presence of a deviation ΔA_3, the value f_V^* does not correspond to the real concentration. When $\Delta A_3 > 0$ (red symbols and letters in Figure 3) the picked-up signal is higher than the one expected assuming linear

behaviour, introducing an error by excess in the estimate of the real concentration, which is no longer f_V^* but some lower value f_V. The true value can be easily determined with the aid of Figure 3 by displacing the intersection point on the calibration line (the black square) downwards along the calibration line until the ordinate takes the value $A_3^{(NI)} \equiv A_3^{(E)} - \Delta A_3$, which defines another intersection point (the red square) allowing one to find the correct value f_V at once. Of course, opposite steps should be followed when $\Delta A_3 < 0$ (blue symbols and letters).

However, this adjustment procedure works only when the value ΔA_3 is known, which is not the case in a real measurement. Therefore, the problem of getting the right concentration from the analysis of the third harmonic should be approached in a different way. In fact, this can be easily done by detecting not only the magnitude A_3 but also the phase shift ϕ_3 of the third harmonic, as shown in the next Subsection.

Adjustment based on the third harmonic

The real concentration of the particles which generate a third-harmonic signal can be obtained by making use of a simple relation between magnitude and phase shift, which derives from the rate equations and is shown in Figure 6. When the deviation ΔA_3 is reported as a function of $\Delta\phi_3^2 \equiv \left(\phi_3^{(E)} - \phi_3^{(NI)}\right)^2$, a linear relation between these two quantities is observed for all examined nanoparticle diameters (the different points represent values of f_V increasing from 0 to 0.03). Therefore, the following linear expression can be proposed:

$$\Delta A_3 = k \left[\phi_3^{(E)} - \phi_3^{(NI)}\right]^2 \tag{6}$$

The angular coefficient k of equation 6 can be either positive or negative, depending on particle size. It is concluded that from a single measurement of the third harmonic it is possible to obtain not only the magnitude $A_3^{(E)}$ but also the correction term ΔA_3 which allows one to modify the measured magnitude and to obtain the correct f_V.
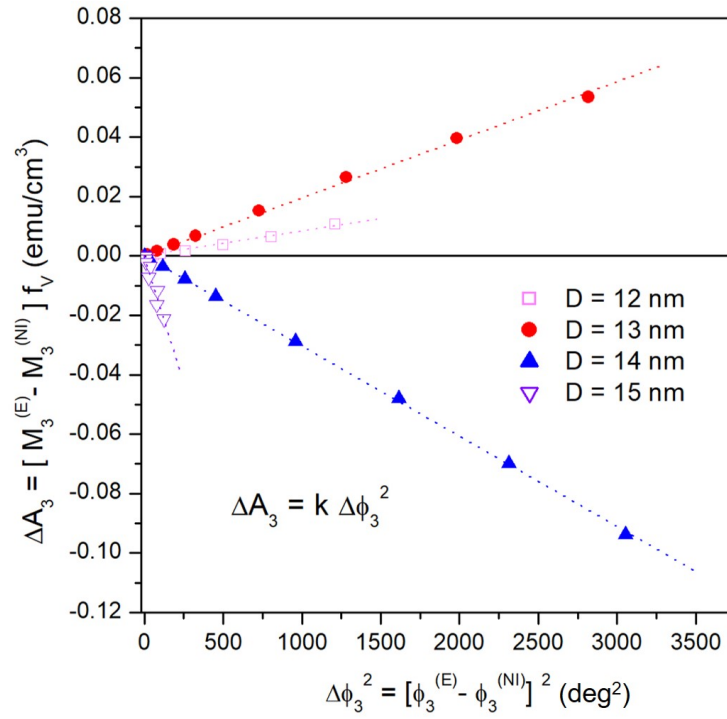
Figure 6: Linear relationship between variation of the magnitude of the third harmonic of the signal with respect to the noninteracting case (ΔA_3) and the square of the variation of the corresponding phase shift ($\Delta\phi_3$).

Outside the interval of particle sizes reported in Figure 6 (12 to 15 nm), $\Delta\phi_3$ quickly drops to zero; in particular, in particles of size less than 12 nm the magnetic response can always be likened to the anhysteretic Langevin function for both interacting and noninteracting systems, so that $\phi_3 \to 0$ (and therefore $\Delta\phi_3 \to 0$), whilst in particles larger than 15 nm the energy barrier for noninteracting particles is already so high that a further increase due to dipolar interaction does not affect the magnetic response, so that magnitude and phase of the third harmonic are independent of f_V, hence again $\Delta\phi_3 \to 0$.

A proof of concept

The validity of the adjustment procedure proposed in the previous Section can be tested in a simplified case serving as a proof of concept.

In a MPI scanning operation, the high-frequency signal picked up at the instantaneous FFP is determined not only by the nanoparticles actually located at the FFP (where the bias field is vanishingly small) but also by the ones present in neighbouring regions of tissue where the bias field is not strong enough to saturate the particle magnetization, making it necessary to solve a complex inversion problem in order to properly analyse the convoluted signal generated by the target.[3,77,78] The higher the gradient of the bias field, the less convoluted is the picked-up signal. In the limit of an infinite gradient, all particles not precisely located at the FFP are magnetically saturated and therefore produce no magnetic signal at the driving field frequency. Such an ideal limit is precisely the one exploited here in a proof of concept aimed to test the adjustment strategy.

Let us consider an uneven distribution of magnetic nanoparticles on a reference (x, y) plane, such as the one depicted in the top panel of Figure 7. The volume concentration $f_V(x, y)$ takes a small constant value ($f_V = 0.001$) almost everywhere except in proximity of two "accumulation points", where it attains much higher maximum levels (equal to 0.01

and 0.025, respectively). The distribution of $f_V(x, y)$ around the two accumulation points is described by two bidimensional Gaussian curves (note the concentration contour maps projected on the top of the panel). The base value of f_V is such that nanoparticles can be safely considered as noninteracting: however, this is no longer true near the accumulation points.

The middle panels of Figure 7 show the unadjusted estimates of the nanoparticle concentration obtained for two diameter values D by using the linear law $A_3 = h f_V$ - which amounts to assume that nanoparticles are noninteracting everywhere in the plane. In both cases, the estimate turns out to be correct near to the boundaries but it is wrong in proximity of the two accumulation points: the highest mismatch between real and estimated values is observed at the accumulation point where f_V is highest, as expected; moreover, when $D = 13$ nm the estimate is wrong by excess, whilst when $D = 14$ nm an error by defect is observed (these results reflect the behaviour of the $A_3(f_V)$ curves drawn in Figure 4).

The lower panels show the estimates after performing the adjustment through Eq. 6. To this aim, both magnitude and phase shift of the third harmonic of the signal were collected at all points on the (x, y) plane. The agreement between the adjusted estimates and the starting f_V distribution turns out to be excellent everywhere.

The validity of the adjustment procedure can be checked in Figure 8, where real and estimated f_V distributions are shown for different particle diameters along the section of the (x, y) plane of Figure 7 corresponding to $y = 0$. In all cases, the unadjusted estimate curves fail to reproduce the actual Gaussian distributions close to the accumulation points (with a larger error systematically observed around the region where the actual f_V is highest); note that prior to adjustment the third harmonic definitely fails to reproduce the actual shape of the f_V distribution for large particle diameters, showing a profile much flatter than the actual one around the accumulation points.
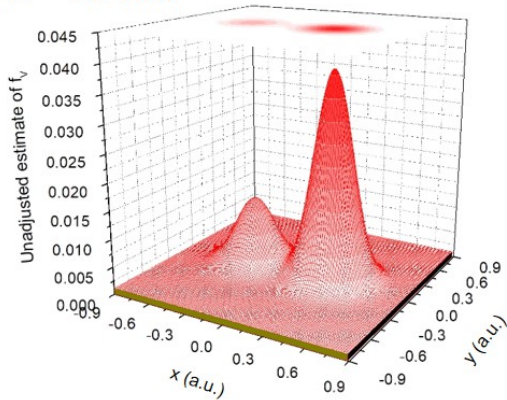
On the contrary, after adjustment all estimates become precisely coincident in both magnitude and shape with the starting f_V curve. No free parameters are used to obtain the

Actual MNPs distribution
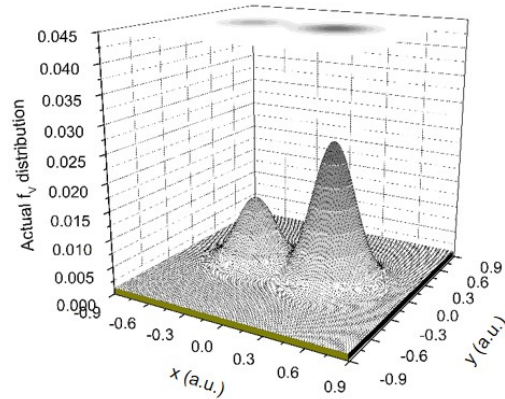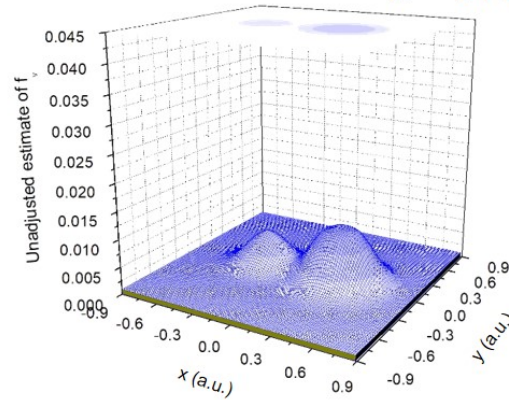

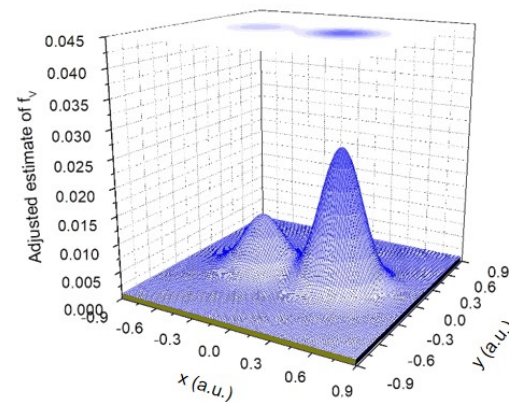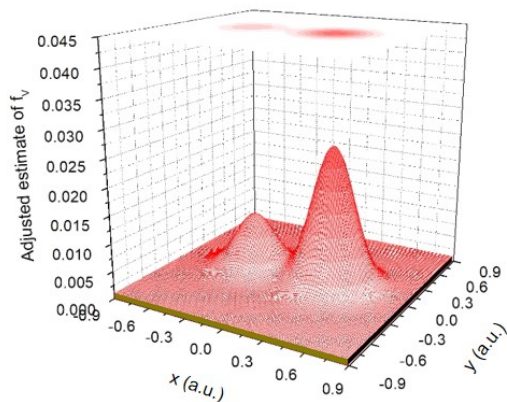## Unadjusted estimate

D = 13 nm

D = 14 nm

Adjusted estimate

Figure 7: Proof of concept of the validity of the proposed adjustment technique.Top panel: real nanoparticle distribution in two dimensions, $f_V(x, y)$. Middle panels: incorrect estimates of f_V obtained if magnetic interactions are neglected; lower panels: correct estimates of f_V resulting after adjustment.

adjusted curves of Figure 8, the angular coefficient k of Eq. 6 being univocally determined by the output of the rate-equation calculations (see Figure 6 for some typical diameters).
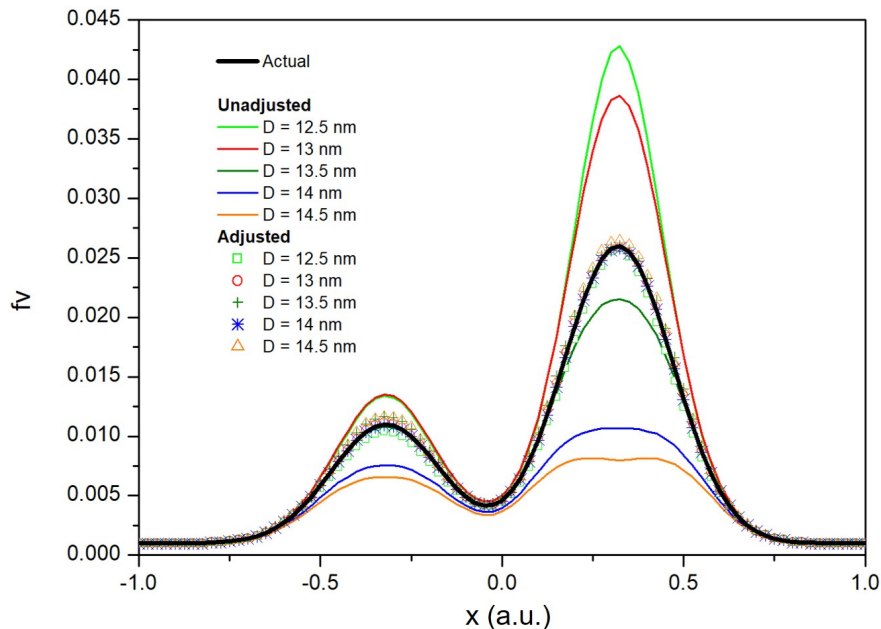
Figure 8: Cross section along the $y = 0$ plane of the curves shown in Figure 7. Curves for additional values of D are also shown.

Polydisperse nanoparticles

In the experimental practice and in common applications magnetic nanoparticles are never rigorously monodisperse. Owing to the strong impact of nanoparticle size not only on their magnetic response but also on their hydrodynamic properties and toxicity,[79–81] using a sufficiently narrow distribution of particle diameters is often the best choice.

As a consequence, the validity of the adjustment procedure has been checked on a lognormal distribution of D values with mode $D_C = 12.5$ nm and standard deviation $w = 0.07$. The distribution is shown in Figure 9 (panel a), left side); only diameters between 10 and 15 nm are to be taken into consideration in the average.

The calculation is done according to a procedure outlined elsewhere.[31] The magnitude of the third-harmonic signal is reported as a function of f_V in Figure 9 (panel (a), upper right

Figure 9: Case of polydisperse particles: a) Lognormal distribution of particle sizes and resulting average behaviour of A_3 and ϕ_3; b)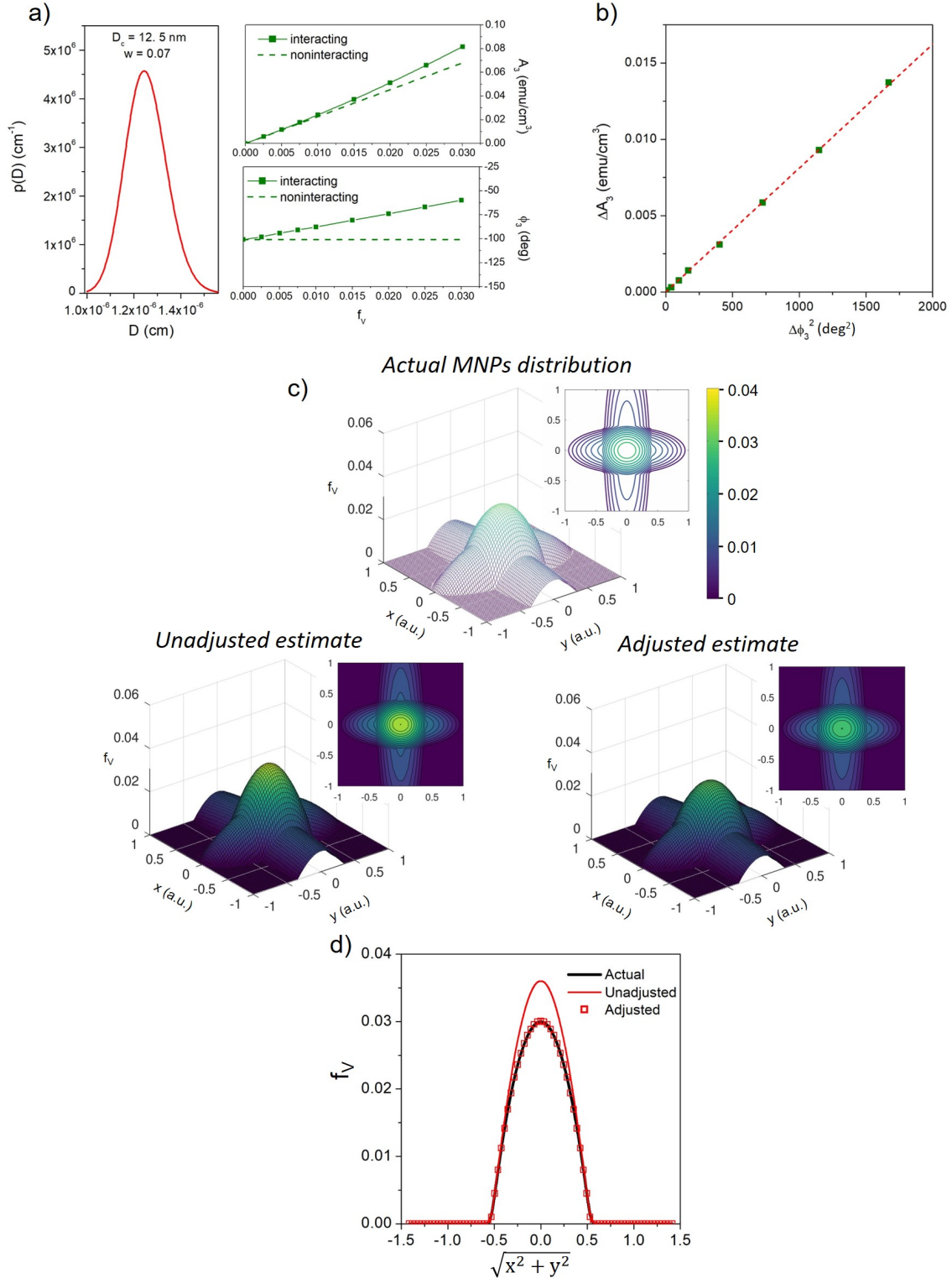 linear relation between ΔA_3 and $(\Delta\phi_3)^2$; c) proof of concept of the adjustment technique making use of a more complex arrangement of particles in two dimensions; d) cross section of the estimated values of f_V along the $y = x$ plane.

side): the full line refers to the interacting system while the dashed straight line describes noninteracting particles. Although the diameters involved in the average are both higher and lower than $D_{NI}^{(max)}$ (see Eq. 4), A_3 turns out to be still enhanced with respect to $A_3^{(NI)}$. The behaviour of ϕ_3 as a function of f_V is reported in panel a), lower right side: full/dashed lines refer to the interacting/noninteracting case. Even in the presence of a distribution of particle diameters, the quantity ΔA_3 turns out to be a linear function of $\Delta\phi_3^2$, as shown in panel b).

Such a linear relationship allows one to implement the same adjustment procedure outlined in Section for monodisperse particles. The validity of the method is demonstrated by a second proof of concept based on a different, more complex arrangement of accumulating particles, as shown in panel (c) of Figure 9. In this case, the $f_V(x, y)$ function is equal to zero everywhere outside two ellipses with perpendicular major axes; inside, the concentration takes values described by a parabolic law whose maximum is on the major axis of the ellipse. Estimates of f_V resulting from analysis of the third harmonic of $M(t)$ without and with adjustment are shown: once again, the unadjusted estimate fails to correctly reproduce the actual f_V distribution in regions where dipolar interaction can be no longer neglected. The excellent agreement between adjusted estimate and real $f_V(x, y)$ distribution is put in evidence by the rightmost plot of panel (c), where a transverse section of $f_V(x, y)$ is drawn along the $y = x$ diagonal line.

Conclusions

In-depth knowledge of the magnetic behaviour of nanoparticles eligible as tracers for MPI is instrumental to correctly apply such a powerful imaging technique to precisely measure their local concentration in a tissue.

In this paper, rate equations were exploited to extract the magnitude and phase of the

third harmonic of the $M(t)$ signal generated from tracers submitted to a harmonic magnetic field $H(t)$. Extraction and analysis of the third harmonic of the induced voltage is a typical feature of present-day MPI operating techniques.

Although the present treatment makes use of rather ideal systems (e.g, spherical nanoparticles of magnetite with purely uniaxial anisotropy; no surface or core-shell effects; absence of formation either of tightly packed nanoparticle aggregates or chains), some conclusions of general interest can be drawn:

a) magnetic hysteresis is not only a property of magnetically blocked nanoparticles having a size larger than the critical size for the onset of superparamagnetism at room temperature: even particles behaving as superparamagnetic in a quasi-static measurement display a hysteresis when operating at high frequency, as for instance in MPI applications;

b) neglecting the hysteretic properties of magnetic tracers can lead to inadequate modelling of their magnetic response: interpretation schemes making explicit reference to the Langevin function should therefore be considered as merely qualitative;

c) magnetic dipole-dipole interaction can play a role even when tracers are almost evenly distributed in the tissue (i.e., without giving rise to tight aggregates). Such an interaction brings about an increase of the height of the energy barrier of the DWS, and therefore strongly affects magnetization switching; this in turn brings about substantial changes in the shape and width of magnetic hysteresis loops and in the magnitude and phase of the third harmonic; dipolar interaction increases linearly with increasing nanoparticle concentration;

d) usually, measuring the magnitude of the third harmonic of the signal is believed to be enough to estimate the local concentration f_V of tracers in a typical MPI scanning operation mode; this can be a good standpoint when the shape of the $M(t)$ waveform (or equivalently of the $M(H)$ curve) is virtually unaffected by the concentration itself. Indeed, the method works well at sufficiently low tracer concentrations, as in many applications of MPI. However, this is no longer true when MPI is used in combination of applications requiring a larger

local concentration of nanoparticles (such as MPI-assisted magnetic hyperthermia) or in all circumstances where an unpredictable local accumulation of particles can occur; in these cases, neglecting dipolar interaction can lead to a mismatch between the real concentration of particles and its estimate by MPI;

e) a method to cope with this difficulty by using not only the magnitude but also the phase shift of the third harmonic is proposed; a simple formula allows one to obtain the correct f_V distribution even in the presence of non-negligible dipolar interactions among tracers. The adjustment procedure has been shown to work well both for monodisperse and polydisperse nanoparticle systems and has been checked on different distributions of nanoparticles on a plane.

Although the model's assumptions do not exactly match the properties of commercial iron oxide nanotracers (whose shape is not perfectly spherical and whose magnetic anisotropy has cubic, rather than uniaxial symmetry), the present conclusions are helpful in correctly identifying the factors which most affect their efficiency for MPI and in determining the range of sizes and the measuring procedures which guarantee the best performance in the experimental practice.

The present results can be naturally extended to the case of a large, non-infinite gradient of the bias field applied to the target. In such a more realistic case, the signal picked up at the FFP is convoluted with weaker but definitely nonzero signals contributed by nearby areas of the target; the adjustment method combining magnitude and phase shift of the third harmonic should be incorporated in the analysis of all signals in such a way that the ensuing deconvolution procedure should include the prescriptions outlined and discussed in this work.

Appendix

Analytic solution for collinear nanoparticles

In the collinear case the expression of all quantities entering the rate equations are greatly simplified, allowing analytic solutions to be found.[41,65] For the sake of simplicity, the treatment is limited here to the case of noninteracting nanoparticles.

The magnetization of an assembly of monodisperse, collinear nanoparticles, $M(t)$, is proportional to the number of particles instantaneously found in well 1 of the DWS, $N_1(t)$: using $n_1(t) = \frac{N_1}{N} \equiv \frac{N_1}{N_1+N_2}$, one has $M(t) = M_s(2n_1(t) - 1)$.[41] The rate equation for n_1 is:[41]

$$\frac{dn_1}{dt} = \frac{1}{\tau_2} - \left(\frac{1}{\tau_1} + \frac{1}{\tau_2}\right)n_1 \equiv c_2(t) - c_1(t)n_1(t) \tag{7}$$

where:

$$c_1(t) = \frac{1}{\tau_2(t)} = \frac{1}{\tau_0}\exp\left[\frac{\left(K_uV + \frac{M_s^2H_V^2V}{8K_u}\right) - M_sH_VV\cos(\omega t) + \frac{M_s^2H_V^2V}{8K_u}\cos(2\omega t)}{k_BT}\right]$$

and

$$c_2(t) = \frac{1}{\tau_1(t)} + \frac{1}{\tau_2(t)} = \frac{2}{\tau_0}\exp\left[\frac{\left(K_uV + \frac{M_s^2H_V^2V}{8K_u}\right) - \frac{M_s^2H_V^2V}{8K_u}\cos(2\omega t)}{k_BT}\right]\cosh\left[\frac{M_sH_VV}{k_BT}\cos(\omega t)\right]$$

where $\omega = 2\pi f$. These are exact expressions of the rate equation coefficients. Using the Taylor development of the exponential functions and recursive analytical formulas to express powers of $\cos(\omega t)/\cos(2\omega t)$ in terms of cosines of multiple arguments $\cos(k\omega t)$ with $k \geq 2$, the above quantities can be developed in two cosine Fourier series as:

$$c_1(t) = \sum_{k=0}^{\infty} a_k \cos(k\omega t)$$

$$c_2(t) = \sum_{k=0}^{\infty} b_k \cos(k\omega t)$$

All a_k, b_k coefficients turn out to be expressed as series of powers of known parameters. Here we give the explicit expressions of the leading terms of the development of two coefficients, a_3 and b_0, which are of particular relevance in the present study:

$$a_3 = -\frac{M_s^3 H_V^3 V^2}{16 K_u (k_B T)^2} + \frac{\frac{M_s^3 H_V^3 V^3}{24} - \frac{M_S^2 H_V^4 V^3}{32 K_u} + \frac{M_s^5 H_V^5 V^3}{512 K_u^2}}{(k_B T)^3} + \ldots \tag{8}$$

$$b_0 = 1 + \frac{1}{4}\left(\frac{M_s^2 H_V^2 V}{8 K_u k_B T}\right)^2 + \frac{1}{4}\left(\frac{M_s H_V V}{k_B T}\right)^2 + \frac{1}{64}\left(\frac{M_s H_V V}{k_B T}\right)^4 + \ldots \tag{9}$$

The solution of the rate equation for $n_1(t)$ is:

$$n_1(t) = f_0\, e^{-2b_0 f_0 t} \sum_{k=0}^{\infty} a_n \int \cos(k\omega t) e^{2b_0 f_0 t} dt + const. \tag{10}$$

where $f_0 = \frac{1}{\tau_0} \exp\left(-\frac{K_u V + \frac{M_s^2 H_V^2 V}{8 K_u}}{k_B T}\right)$. In Eq. 10 only the first term of the Fourier development for $c_2(t)$ has been retained, higher order terms corresponding to a ripple superimposed to the dominant exponential terms of the type $\exp(\pm 2b_0 f_0 t)$ appearing in the Equation. This is the only approximation involved in the present analytic treatment. The third-order harmonic $n_1^{[3]}(t)$ is just:

$$n_1^{[3]}(t) = f_0 \, e^{-2b_0 f_0 t} a_3 \int \cos(3\omega t) e^{2b_0 f_0 t} dt =$$

$$= \frac{a_3 f_0}{(4b_0^2 f_0^2 + 9\omega^2)} \left[(2b_0 f_0 \cos(3\omega t) - 3\omega \sin(3\omega t) \right] =$$

$$= \frac{a_3 f_0}{(4b_0^2 f_0^2 + 9\omega^2)^{1/2}} \cos(3\omega t - \phi_3), \quad (11)$$

where a_3 and b_0 are given in Eqs. 8 and 9. The phase shift of the third harmonic with respect to $H(t)$ ($\phi_3 = \arctan\left[\frac{3\omega}{2b_0 f_0}\right]$) appears by effect of the integration. The magnitude of the third harmonic of the magnetization $M(t)$ is therefore:

$$M_3 = 2M_s \frac{a_3 f_0}{(4b_0^2 f_0^2 + 9\omega^2)^{1/2}}. \quad (12)$$

For a given frequency f of the driving field, M_3 exhibits a sharp maximum as a function of particle diameter D, which is located at $D = D_{NI}^{(max)}$ defined in Eq. 4. With the current parameter values, $D_{NI}^{(max)} \simeq 13.4$ nm for collinear easy axes. The expression of $D_{NI}^{(max)}$ is obtained considering the behaviour with D of the function:

$$\frac{f_0}{(4b_0^2 f_0^2 + 9\omega^2)^{1/2}}$$

which appears in Eq. 12 and takes values between $\frac{1}{2}$ (for $D \to 0, f_o \to \infty$) and 0 (for $D \to \infty, f_0 \to 0$). This is almost a step function because of the presence of the exponential term in f_0, and drops very rapidly from the initial value to zero. $D_{NI}^{(max)}$ closely corresponds to the diameter where the function takes exactly one half of the initial value. Below $D_{NI}^{(max)}$, M_3 increases because of the increasing behaviour of a_3; above $D_{NI}^{(max)}$, M_3 quickly disappears. Although Eq. 12 has been derived for collinear particles, this analytical solution closely reproduces the main features of the numerical solution for an assembly of particles with random easy axes (shown in Figure 5). The value of $D_{NI}^{(max)}$ given by Eq. 4 turns out to be a good estimate of the position of the actual maximum of M_3.

Finding an explicit expression for $D_{NI}^{(max)}$ for a given driving-field frequency and amplitude is helpful in applications involving interacting particles: as a rule of thumb, if $D < D_{NI}^{(max)}$, the measured value of $A_3 = M_3 f_V$ is higher than the one predicted by calibration, the contrary being true for $D > D_{NI}^{(max)}$. When dipolar interaction is switched on $D^{(max)}$ decreases, as checked by inserting $K_{eff} = K_u + \alpha M_s^2$ in Eq. 4. The linear relation reported in Eq. 5 is immediately obtained from Eq. 4 when $\alpha M_s^2 << K_u$, as is usually the case.

The comparison between the analytic expression of M_3 and the output of numerical calculation in the collinear case is reported as Supporting Information.

Funding

Notes

The authors declare no competing financial interest.

Supporting Information Available

Additional details including: rate equation framework, third harmonic's phase shift at equilibrium, analytical results in collinear case.

References

(1) Gleich, B. *Principles and Applications of Magnetic Particle Imaging*; Springer Vieweg: Wiesbaden, 2014.

(2) Bakenecker, A.; Ahlborg, M.; Debbeler, C.; Kaethner, C.; Lüdtke-Buzug, K. In *Pre-*

cision Medicine: Tools and Quantitative Approaches; Deigner, H.-P., Kohl, M., Eds.; Academic Press, 2018; Chapter 9, pp 183–228.

(3) Enpuku, K.; Yoshida, T. In *Bioimaging*; Ueno, S., Ed.; CRC Press: Boca Raton, 2020; Chapter 7, pp 155–183.

(4) Bente, K.; Bakenecker, A.; von Gladiss, A.; Bachmann, F.; Cebers, A.; Buzug, T.; Faivre, D. Selective Actuation and Tomographic Imaging of Swarming Magnetite Nanoparticles. *ACS Applied Nano Materials* **2021**, *4*, 6752–6759.

(5) Talebloo, N.; Gudi, M.; Robertson, N.; Wang, P. Magnetic Particle Imaging: Current Applications in Biomedical Research. *Journal of Magnetic Resonance Imaging* **2020**, *51*, 1659–1668.

(6) Han, X.; Li, Y.; Liu, W.; Chen, X.; Song, Z.; Wang, X.; Deng, Y.; Tang, X.; Jiang, Z. The applications of magnetic particle imaging: From cell to body. *Diagnostics* **2020**, *10*, 1–12.

(7) https://www.magneticinsight.com/applications/.

(8) Hildebrand, S.; Löwa, N.; Paysen, H.; Fratila, R.; Reverte-Salisa, L.; Trakoolwilai-wan, T.; Niu, Z.; Kasparis, G.; Preuss, S.; Kosch, O.; M. De La Fuente, J.; Thanh, N.; Wiekhorst, F.; Pfeifer, A. Quantification of Lipoprotein Uptake in Vivo Using Magnetic Particle Imaging and Spectroscopy. *ACS Nano* **2021**, *15*, 434–446.

(9) Sehl, O. C.; Gevaert, J. J.; Melo, K. P.; Knier, N. N.; Foster, P. J. A perspective on cell tracking with magnetic particle imaging. *Tomography* **2020**, *6*, 315–324.

(10) Wang, Q.; Ma, X.; Liao, H.; Liang, Z.; Li, F.; Tian, J.; Ling, D. Artificially Engineered Cubic Iron Oxide Nanoparticle as a High-Performance Magnetic Particle Imaging Tracer for Stem Cell Tracking. *ACS Nano* **2020**, *14*, 2053–2062.

(11) Parkins, K. M.; Melo, K. P.; Chen, Y.; Ronald, J. A.; Foster, P. J. Visualizing tumour self-homing with magnetic particle imaging. *Nanoscale* **2021**, *13*, 6016–6023.

(12) Tay, Z. W.; Chandrasekharan, P.; Fellows, B. D.; Arrizabalaga, I. R.; Yu, E.; Olivo, M.; Conolly, S. M. Magnetic particle imaging: An emerging modality with prospects in diagnosis, targeting and therapy of cancer. *Cancers* **2021**, *13*, 1–27.

(13) Ludewig, P.; Szwargulski, P.; Wilmes, M.; Javidi, E.; Thieben, F.; Graeser, M.; Koch, M.; Gruettner, C.; Adam, G.; Gerloff, C.; Magnus, T.; Knopp, T. Monitoring intracranial cerebral hemorrhage using multicontrast real-time magnetic particle imaging. *ACS Nano* **2020**, *14*, 13913–13923.

(14) Tay, Z. W.; Chandrasekharan, P.; Chiu-Lam, A.; Hensley, D. W.; Dhavalikar, R.; Zhou, X. Y.; Yu, E. Y.; Goodwill, P. W.; Zheng, B.; Rinaldi, C.; Conolly, S. M. Magnetic Particle Imaging-Guided Heating in Vivo Using Gradient Fields for Arbitrary Localization of Magnetic Hyperthermia Therapy. *ACS Nano* **2018**, *12*, 3699–3713.

(15) Lu, Y.; Rivera-Rodriguez, A.; Tay, Z. W.; Hensley, D.; Fung, K. L.; Colson, C.; Saayujya, C.; Huynh, Q.; Kabuli, L.; Fellows, B.; Chandrasekharan, P.; Rinaldi, C.; Conolly, S. Combining magnetic particle imaging and magnetic fluid hyperthermia for localized and image-guided treatment. *International Journal of Hyperthermia* **2020**, *37*, 141–154.

(16) Wells, J.; Twamley, S.; Sekar, A.; Ludwig, A.; Paysen, H.; Kosch, O.; Wiekhorst, F. Lissajous scanning magnetic particle imaging as a multifunctional platform for magnetic hyperthermia therapy. *Nanoscale* **2020**, *12*, 18342–18355.

(17) Chandrasekharan, P.; Tay, Z. W.; Hensley, D.; Zhou, X. Y.; Fung, B. K.; Colson, C.; Lu, Y.; Fellows, B. D.; Huynh, Q.; Saayujya, C.; Yu, E.; Orendorff, R.; Zheng, B.; Goodwill, P.; Rinaldi, C.; Conolly, S. Using magnetic particle imaging systems to local-

ize and guide magnetic hyperthermia treatment: Tracers, hardware, and future medical applications. *Theranostics* **2020**, *10*, 2965–2981.

(18) Bobo, D.; Robinson, K. J.; Islam, J.; Thurecht, K. J.; Corrie, S. R. Nanoparticle-Based Medicines: A Review of FDA-Approved Materials and Clinical Trials to Date. *Pharmaceutical Research* **2016**, *33*, 2373–2387.

(19) Knopp, T.; Gdaniec, N.; Möddel, M. Magnetic particle imaging: From proof of principle to preclinical applications. *Physics in Medicine and Biology* **2017**, *62*, R124–R178.

(20) Guzy, J.; Chakravarty, S.; Buchanan, F.; Chen, H.; Gaudet, J.; Hix, J.; Mallett, C.; Shapiro, E. Complex Relationship between Iron Oxide Nanoparticle Degradation and the Signal Intensity in Magnetic Particle Imaging. *ACS Applied Nano Materials* **2020**, *3*, 3991–3999.

(21) Zhou, X. Y.; Tay, Z. W.; Chandrasekharan, P.; Yu, E. Y.; Daniel, W.; Orendorff, R.; Jeffris, K. E.; Mai, D.; Zheng, B.; Patrick, W.; Conolly, S. M. Magnetic Particle Imaging for Radiation-Free, Sensitive and High-Contrast Vascular Imaging and Cell Tracking. *Current Opinion in Chemical Biology* **2019**, *45*, 131–138.

(22) Wu, K.; Su, D.; Saha, R.; Liu, J.; Chugh, V.; Wang, J.-P. Magnetic Particle Spectroscopy: A Short Review of Applications Using Magnetic Nanoparticles. *ACS Applied Nano Materials* **2020**, *3*, 4972–4989.

(23) Müssig, S.; Granath, T.; Schembri, T.; Fidler, F.; Haddad, D.; Hiller, K.-H.; Wintzheimer, S.; Mandel, K. Anisotropic Magnetic Supraparticles with a Magnetic Particle Spectroscopy Fingerprint as Indicators for Cold-Chain Breach. *ACS Applied Nano Materials* **2019**, *2*, 4698–4702.

(24) Wilhelm, S.; Tavares, A. J.; Dai, Q.; Ohta, S.; Audet, J.; Dvorak, H. F.; Chan, W. C. Analysis of nanoparticle delivery to tumours. *Nature Reviews Materials* **2016**, *1*, 1–12.

(25) Xiong, F.; Huang, S.; Gu, N. Magnetic nanoparticles: recent developments in drug delivery system. *Drug Development and Industrial Pharmacy* **2018**, *44*, 697–706.

(26) Wei, Y.; Quan, L.; Zhou, C.; Zhan, Q. Factors relating to the biodistribution & clearance of nanoparticles & their effects on in vivo application. *Nanomedicine* **2018**, *13*, 1495–1512.

(27) Lee, K.; David, A. E.; Zhang, J.; Shin, M. C.; Yang, V. C. Enhanced accumulation of theranostic nanoparticles in brain tumor by external magnetic field mediated in situ clustering of magnetic nanoparticles. *Journal of Industrial and Engineering Chemistry* **2017**, *54*, 389–397.

(28) Paysen, H.; Loewa, N.; Weber, K.; Kosch, O.; Wells, J.; Schaeffter, T.; Wiekhorst, F. Imaging and quantification of magnetic nanoparticles: Comparison of magnetic resonance imaging and magnetic particle imaging. *Journal of Magnetism and Magnetic Materials* **2019**, *475*, 382–388.

(29) Liu, J.; Jang, B.; Issadore, D.; Tsourkas, A. Use of Magnetic Fields and Nanoparticles to Trigger Drug Release and Improve Tumor Targeting. *Wiley Interdisciplinary Reviews: Nanomedicine and Nanobiotechnology* **2019**, *11*, e1571.

(30) Rezanezhad, A.; Hajalilou, A.; Eslami, F.; Parvini, E.; Abouzari-Lotf, E.; Aslibeiki, B. Superparamagnetic magnetite nanoparticles for cancer cells treatment via magnetic hyperthermia: effect of natural capping agent, particle size and concentration. *Journal of Materials Science: Materials in Electronics* **2021**, *32*, 24026–24040.

(31) Barrera, G.; Allia, P.; Tiberto, P. Dipolar interactions among magnetite nanoparticles for magnetic hyperthermia: A rate-equation approach. *Nanoscale* **2021**, *13*, 4103–4121.

(32) Mitchell, M. J.; Billingsley, M. M.; Haley, R. M.; Wechsler, M. E.; Peppas, N. A.; Langer, R. Engineering precision nanoparticles for drug delivery. *Nature Reviews Drug Discovery* **2021**, *20*, 101–124.

(33) Pablico-Lansigan, M. H.; Situ, S. F.; Samia, A. C. S. Magnetic particle imaging: Advancements and perspectives for real-time in vivo monitoring and image-guided therapy. *Nanoscale* **2013**, *5*, 4040–4055.

(34) Paysen, H.; Wells, J.; Kosch, O.; Steinhoff, U.; Trahms, L.; Schaeffter, T.; Wiekhorst, F. Towards quantitative magnetic particle imaging: A comparison with magnetic particle spectroscopy. *AIP Advances* **2018**, *8*, 10–15.

(35) Paysen, H.; Loewa, N.; Stach, A.; Wells, J.; Kosch, O.; Twamley, S.; Makowski, M. R.; Schaeffter, T.; Ludwig, A.; Wiekhorst, F. Cellular uptake of magnetic nanoparticles imaged and quantified by magnetic particle imaging. *Scientific Reports* **2020**, *10*, 1–8.

(36) Pimlott, S. L.; Sutherland, A. Molecular tracers for the PET and SPECT imaging of disease. *Chemical Society Reviews* **2011**, *40*, 149–162.

(37) Murase, K.; Shimada, K. Lock-in-Amplifier Model for Analyzing the Behavior of Signal Harmonics in Magnetic Particle Imaging. *Open Journal of Applied Sciences* **2018**, *08*, 170–183.

(38) Yu, E. Y.; Chandrasekharan, P.; Berzon, R.; Tay, Z. W.; Zhou, X. Y.; Khandhar, A. P.; Ferguson, R. M.; Kemp, S. J.; Zheng, B.; Goodwill, P. W.; Wendland, M. F.; Krishnan, K. M.; Behr, S.; Carter, J.; Conolly, S. M. Magnetic Particle Imaging for Highly Sensitive, Quantitative, and Safe in Vivo Gut Bleed Detection in a Murine Model. *ACS Nano* **2017**, *11*, 12067–12076.

(39) Wu, X. L.; Zhang, X. Y.; Steinberg, X. G.; Qu, X. H.; Huang, X. S.; Cheng, X. M.; Bliss, X. T.; Du, X. F.; Rao, X. J.; Song, X. G.; Pisani, X. L.; Doyle, X. T.; Conolly, X. S.; Krishnan, X. K.; Grant, X. G.; Wintermark, X. M. A review of magnetic particle imaging and perspectives on neuroimaging. *American Journal of Neuroradiology* **2019**, *40*, 206–212.

(40) Cullity, B. D.; Graham, C. D. *Introduction to Magnetic Materials*; 2009.

(41) Allia, P.; Barrera, G.; Tiberto, P. Hysteresis effects in magnetic nanoparticles: A simplified rate-equation approach. *Journal of Magnetism and Magnetic Materials* **2020**, *496*, 165927.

(42) Lu, C.; Han, L.; Wang, J.; Wan, J.; Song, G.; Rao, J. Engineering of magnetic nanoparticles as magnetic particle imaging tracers. *Chemical Society Reviews* **2021**, *50*, 8102–8146.

(43) Tomitaka, A.; Koshi, T.; Hatsugai, S.; Yamada, T.; Takemura, Y. Magnetic characterization of surface-coated magnetic nanoparticles for biomedical application. **2011**, *323*, 1398–1403.

(44) Song, G.; Kenney, M.; Chen, Y. S.; Zheng, X.; Deng, Y.; Chen, Z.; Wang, S. X.; Gambhir, S. S.; Dai, H.; Rao, J. Carbon-coated FeCo nanoparticles as sensitive magnetic-particle-imaging tracers with photothermal and magnetothermal properties. *Nature Biomedical Engineering* **2020**, *4*, 325–334.

(45) Them, K. On magnetic dipole-dipole interactions of nanoparticles in magnetic particle imaging. *Physics in Medicine and Biology* **2017**, *62*, 5623–5639.

(46) Teeman, E.; Shasha, C.; Evans, J. E.; Krishnan, K. M. Intracellular dynamics of superparamagnetic iron oxide nanoparticles for magnetic particle imaging. *Nanoscale* **2019**, *11*, 7771–7780.

(47) Etemadi, H.; Plieger, P. G. Magnetic fluid hyperthermia based on magnetic nanoparticles: Physical characteristics, historical perspective, clinical trials, technological challenges, and recent advances. *Advanced Therapeutics* **2020**, *3*, 1–49.

(48) Jiang, Z.; Shan, K.; Song, J.; Liu, J.; Rajendran, S.; Pugazhendhi, A.; Jacob, J. A.; Chen, B. Toxic effects of magnetic nanoparticles on normal cells and organs. *Life Sciences* **2019**, *220*, 156–161.

(49) Gaharwar, U. S.; Meena, R.; Rajamani, P. Biodistribution, clearance and morphological alterations of intravenously administered iron oxide nanoparticles in male wistar rats. *International Journal of Nanomedicine* **2019**, *14*, 9677–9692.

(50) Chrishtop, V. V.; Mironov, V. A.; Prilepskii, A. Y.; Nikonorova, V. G.; Vinogradov, V. V. Organ-specific toxicity of magnetic iron oxide-based nanoparticles. *Nanotoxicology* **2021**, *15*, 167–204.

(51) Mørup, S.; Hansen, M. F.; Frandsen, C. Magnetic interactions between nanoparticles. *Beilstein Journal of Nanotechnology* **2010**, *1*, 182–190.

(52) Wu, K.; Su, D.; Saha, R.; Liu, J.; Wang, J.-P. Investigating the effect of magnetic dipole-dipole interaction on magnetic particle spectroscopy: Implications for magnetic nanoparticle-based bioassays and magnetic particle imaging. *Journal of Physics D: Applied Physics* **2019**, *52*.

(53) Schmool, D. S.; Schmalzl, M. Magnetic Dipolar Interactions in Nanoparticle Systems: Theory, Simulations and Ferromagnetic Resonance. *Springer Proceedings in Physics* **2009**, *122*, 321–326.

(54) Barrera, G.; Allia, P.; Tiberto, P. Heating ability modulation by clustering of magnetic particles for precision therapy and diagnosis. *Journal of Physics D: Applied Physics* **2021**, *54*, 315003.

(55) Soukup, D.; Moise, S.; Céspedes, E.; Dobson, J.; Telling, N. In situ measurement of magnetization relaxation of internalized nanoparticles in live cells. *ACS Nano* **2015**, *9*, 231–240.

(56) Lowa, N.; Seidel, M.; Radon, P.; Wiekhorst, F. Magnetic nanoparticles in different biological environments analyzed by magnetic particle spectroscopy. *Journal of Magnetism and Magnetic Materials* **2017**, *427*, 133–138.

(57) Wu, K.; Tu, L.; Su, D.; Wang, J.-P. Magnetic dynamics of ferrofluids: Mathematical models and experimental investigations. *Journal of Physics D: Applied Physics* **2017**, *50*.

(58) Di Corato, R.; Espinosa, A.; Lartigue, L.; Tharaud, M.; Chat, S.; Pellegrino, T.; Ménager, C.; Gazeau, F.; Wilhelm, C. Magnetic hyperthermia efficiency in the cellular environment fordifferent nanoparticle designs. *Biomaterials* **2014**, *35*, 6400–6411.

(59) Usov, N. A. Numerical simulation of field-cooled and zero field-cooled processes for assembly of superparamagnetic nanoparticles with uniaxial anisotropy. *Journal of Applied Physics* **2011**, *109*, 023913.

(60) Chakraverty, S.; Bandyopadhyay, M.; Chatterjee, S.; Dattagupta, S.; Frydman, A.; Sengupta, S.; Sreeram, P. A. Memory in a magnetic nanoparticle system: Polydispersity and interaction effects. *Physical Review B - Condensed Matter and Materials Physics* **2005**, *71*, 1–8.

(61) Allia, P.; Barrera, G.; Tiberto, P. Nonharmonic Driving Fields for Enhancement of Nanoparticle Heating Efficiency in Magnetic Hyperthermia. *Physical Review Applied* **2019**, *12*, 034041.

(62) Barrera, G.; Allia, P.; Tiberto, P. Temperature-dependent heating efficiency of magnetic nanoparticles for applications in precision nanomedicine. *Nanoscale* **2020**, *12*, 6360–6377.

(63) Rauwerdink, A.; Weaver, J. Harmonic phase angle as a concentration-independent measure of nanoparticle dynamics. *Medical Physics* **2010**, *37*, 2587–2592.

(64) Draack, S.; Lucht, N.; Remmer, H.; Martens, M.; Fischer, B.; Schilling, M.; Ludwig, F.; Viereck, T. Multiparametric Magnetic Particle Spectroscopy of CoFe2O4 Nanoparticles in Viscous Media. *Journal of Physical Chemistry C* **2019**, *123*, 6787–6801.

(65) Allia, P.; Barrera, G.; Tiberto, P. Linearized rate-equation approach for double-well systems: Cooling- and temperature-dependent low-field magnetization of magnetic nanoparticles. *Physical Review B* **2018**, *98*, 134423.

(66) Barrera, G.; Allia, P.; Tiberto, P. Fine tuning and optimization of magnetic hyperthermia treatments using versatile trapezoidal driving-field waveforms. *Nanoscale Advances* **2020**, *2*, 4652–4664.

(67) Kratz, H.; Eberbeck, D.; Wagner, S.; Taupitz, M.; Schnorr, J. Synthetic routes to magnetic nanoparticles for MPI. *Biomed. Tech.* **2013**, *58*, 509–515.

(68) Ferguson, R. M.; Khandhar, A. P.; Krishnan, K. M. Tracer design for magnetic particle imaging (invited). *Journal of Applied Physics* **2012**, *111*.

(69) Hergt, R.; Hiergeist, R.; Hilger, I.; Kaiser, W.; Lapatnikov, Y.; Margel, S.; Richter, U. Maghemite nanoparticles with very high AC-losses for application in RF-magnetic hyperthermia. *Journal of Magnetism and Magnetic Materials* **2004**, *270*, 345–357.

(70) Eberbeck, D.; Wiekhorst, F.; Wagner, S.; Trahms, L. How the size distribution of magnetic nanoparticles determines their magnetic particle imaging performance. *Applied Physics Letters* **2011**, *98*.

(71) Morup, S. Superparamagnetism and Spin Glass Ordering in Magnetic Nanocomposites. *Europhysics letters* **1994**, *28*, 671–676.

(72) Landi, G. T. The random dipolar-field approximation for systems of interacting magnetic particles. *Journal of Applied Physics* **2013**, *113*.

(73) Usov, N. A. Low frequency hysteresis loops of superparamagnetic nanoparticles with uniaxial anisotropy. *Journal of Applied Physics* **2010**, *107*, 123909.

(74) Beola, L.; Gutiérrez, L.; Grazú, V.; Asín, L. In *Nanomaterials for Magnetic and Optical*

Hyperthermia Applications; Fratila, R., De La Fuente, J. M., Eds.; Elsevier Ltd, 2019; pp 317–337.

(75) Maier-Hauff, K.; Ulrich, F.; Nestler, D.; Niehoff, H.; Wust, P.; Thiesen, B.; Orawa, H.; Budach, V.; Jordan, A. Efficacy and safety of intratumoral thermotherapy using magnetic iron-oxide nanoparticles combined with external beam radiotherapy on patients with recurrent glioblastoma multiforme. *Journal of Neuro-Oncology* **2011**, *103*, 317–324.

(76) Griese, F.; Knopp, T.; Gruettner, C.; Thieben, F.; Müller, K.; Loges, S.; Ludewig, P.; Gdaniec, N. Simultaneous Magnetic Particle Imaging and Navigation of large superparamagnetic nanoparticles in bifurcation flow experiments. *Journal of Magnetism and Magnetic Materials* **2020**, *498*, 166206.

(77) Chen, X.; Jiang, Z.; Han, X.; Wang, X.; Tang, X. The Reconstruction of Magnetic Particle Imaging: Current Approaches Based on the System Matrix. *Diagnostics* **2021**, *11*, 773.

(78) Chen, X.; Han, X.; Wang, X.; Liu, W.; Gao, T.; Wang, A.; Tang, X. Simulation of reconstruction based on the system matrix for magnetic particle imaging. *Biomedical Signal Processing and Control* **2022**, *71*, 103171.

(79) Yang, L.; Kuang, H.; Zhang, W.; Aguilar, Z.; Xiong, Y.; Lai, W.; Xu, H.; Wei, H. Size dependent biodistribution and toxicokinetics of iron oxide magnetic nanoparticles in mice. *Nanoscale* **2015**, *7*, 625–636, cited By 104.

(80) Sosnowski, T. Particles on the lung surface - physicochemical and hydrodynamic effects. *Current Opinion in Colloid and Interface Science* **2018**, *36*, 1–9, cited By 24.

(81) Mangal, D.; Conrad, J.; Palmer, J. Nanoparticle dispersion in porous media: Effects of hydrodynamic interactions and dimensionality. *AIChE Journal* **2021**, *67*, 1–14, cited By 1.

TOC Graphic